Evaluation of the radiation field in the future circular collider detector

M. I. Besana,* F. Cerutti, A. Ferrari, W. Riegler, and V. Vlachoudis

European Organisation for Nuclear Research (CERN), CH-1211 Geneva, Switzerland

(Received 10 July 2016; published 21 November 2016)

The radiation load on a detector at a 100 TeV proton-proton collider, that is being investigated within the future circular collider (FCC) study, is presented. A first concept of the detector has been modeled and relevant fluence and dose distributions have been calculated using the FLUKA Monte Carlo code. Distributions of fluence rates are discussed separately for charged particles, neutrons and photons. Dose and 1 MeV neutron equivalent fluence, for the accumulated integrated luminosity, are presented. The peak values of these quantities in the different subdetectors are highlighted, in order to define the radiation tolerance requirements for the choice of possible technologies. The effect of the magnetic field is also discussed. Two shielding solutions have been conceived to minimize the backscattering from the forward calorimeters to the muon chambers and the forward tracking stations. The two possible designs are presented and their effectiveness is discussed.

DOI: 10.1103/PhysRevAccelBeams.19.111004

I. INTRODUCTION

A hadron collider with 100 TeV center-of-mass energy is being investigated within the future circular collider (FCC) study [1] that explores different designs of circular colliders for the post-LHC era. This collider (FCC-hh) is expected to accumulate a data set of 30 ab^{-1} over its lifetime, with peak instantaneous luminosities up to 30×10^{34} cm^{-2} s^{-1}.

The radiation load at the FCC-hh will be more challenging than at the LHC, since the collision energy is seven times higher and the foreseen ultimate instantaneous luminosity is 30 times higher than the nominal LHC one. The integrated luminosity goal exceeds by two orders of magnitude the LHC one [2] and by one order of magnitude the high luminosity LHC (HL-LHC) one [3].

To assess the radiation load on the detector, simulations have been performed using FLUKA [4,5], which is a Monte Carlo code benchmarked up to the TeV energy region and regularly used for beam-machine interaction studies [6], in particular for the LHC and its upgrade.

Similar studies were performed for the LHC experiments in their design phase [7–9] and for their HL-LHC upgrade [10,11], as well as for the experiments that were foreseen at the Very Large Hadron Collider [12] and at the Superconducting Super Collider [13].

Collisions have been simulated taking into account a beam crossing angle of 70 μrad (half) in the vertical plane and a root mean square bunch length of 8 cm.

To optimize the computation time, only half of the detector has been implemented in FLUKA, but the contribution coming from the other half is accounted for. Thanks to the symmetry of the problem, this is achieved by reflecting back particles crossing the $z = 0$ plane. The impact of the backscattering from the target absorber secondaries (TAS), the protection element in front of the final focus triplet, has not been included in this calculation, since, according to the current design of the interaction region [14], the absorber is expected to be outside the experimental cavern and, therefore, adequately shielded.

This paper is organized as follows. In Sec. II the detector concept is discussed and its geometry is described, while the source term is characterized in Sec. III. The obtained results for the radiation load are then presented in Sec. IV and finally the shielding strategies and their effectiveness are discussed in Sec. V.

II. DETECTOR DESCRIPTION

First detector concepts for a 100 TeV proton-proton collider have been established. With the 7-fold increase in center of mass energy with respect to the LHC, a similar energy increase of final state particles from hard scattering events is expected. Therefore the tracker radius R_T is increased by a factor of 2 and the magnetic field B is increased by a factor 1.5 over the numbers from e.g. the CMS experiment, leading to a B R_T^2 increase of 6. The total thickness of a calorimeter, that should absorb the full particle energy, increases with the logarithm of the particle energy, so to contain the seven times more energetic final state particles at the FCC-hh the calorimeter thickness has to be increased by two hadronic interaction lengths λ. These considerations lead to a tracker radius of 2.4 m and total calorimeter thickness of 3.4 m and therefore an inner coil radius of about 6 m. Instead of an iron yoke for return of the magnetic flux, an active shielding coil is assumed.

*maria.ilaria.besana@cern.ch

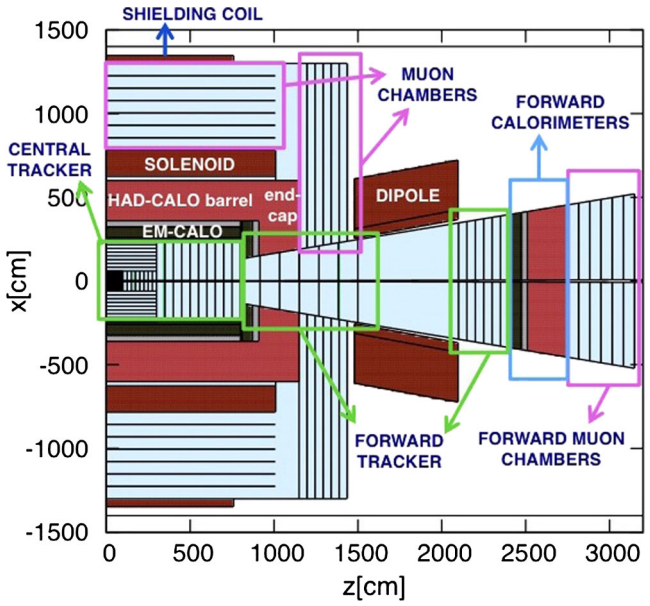

FIG. 1. Detector layout: top view. A detailed description is reported in the text.

The volume between the central and the shielding coil is instrumented with muon chambers.

Since many interesting physics channels, specifically most of the Higgs physics, are highly forward boosted at these high energies, an increase of precision tracking and precision calorimetry from an η range of ± 2.4 at the LHC to an η range of ± 4 for the FCC is assumed, where η is the pseudorapidity, defined as $\eta \equiv -\ln[\tan(\frac{\theta}{2})]$ and θ is the angle between the particle three-momentum $\mathbf{p}$ and the positive direction of the beam axis. Calorimeter acceptance has to be provided even up to possibly $|\eta| = 6$ value in order to be sensitive to the so called vector boson fusion jets. For this reason, two dipoles have been placed in this forward region that provide momentum spectroscopy where the solenoid becomes ineffective.

Figure 1 shows the FCC-hh detector model, as it has been implemented in FLUKA. The x-axis is on the horizontal plane, pointing outside the ring; the y-axis is opposite to gravity and the z-axis is along the beam. The origin of the right-handed coordinate system corresponds to the nominal collision point.

A. Detector geometry and materials

The FCC-hh detector is composed of a cylindrically symmetric central part and a forward part. In the following we give a description of the detector materials and the geometry, as represented in Fig. 1.

1. Central region

The central beampipe is made from beryllium and extends from $z = 0$ to $z = 800$ cm with an inner enveloping radius of 2 cm and a wall thickness of 1 mm.

The tracker of 800 cm half-length has a radial extension from 2.5 cm to 240 cm. All tracker layers are assumed to have 0.43 cm thickness and are made up of 42% C, 30% Polystyrene, 20% Si, 6% Al, 2% Cu, which represents a typical mix of silicon sensor, carbon fiber support structure, cables and services and defines a layer to have 3% of a radiation length X_0.

The first cylindrical tracking layer is placed at $r = 2.5$ cm with a half length of 50 cm. Then follow 8 equidistant cylindrical layers from $r = 7.5$ cm to $r = 60$ cm with half length of 100 cm and 8 equidistant layers from $r = 82.5$ cm to $r = 240$ cm with 300 cm half-length. The rest of the tracker is made up from discs perpendicular to the beampipe, 8 equidistant discs from $z = 125$ cm to $z = 300$ cm with inner radius of 5 cm and outer radius of 60 cm and 10 equidistant discs from $z = 350$ cm to $z = 800$ cm with inner radius of 2.5 cm and outer radius of 240 cm.

The electromagnetic calorimeter (EMCAL) is assumed to use liquid Argon (LAr) technology similar to ATLAS [15] and has a radial extension from $r = 240$ cm to $r = 350$ cm. An aluminium cryostat extending from $r = 250$ cm to $r = 260$ cm is followed by 62 cm of calorimeter, assumed to be a mix of 64.8% liquid Argon, 21.7% Pb, 7.2% Cu, and 6.3% Polystyrene. This layer is then followed by 38 cm of aluminium representing cryostat and electronics.

The hadron calorimeter (HADCAL) extends radially from 360 cm to 600 cm and is assumed to be similar to the ATLAS HCAL [15]. It is composed of homogeneous material assuming 80% Fe and 20% Polystyrene scintillator material.

The magnet coils are extending radially from 625 cm to 782.5 cm and from 1300 cm to 1350 cm and the assumed material is aluminium. The space between the two coils is filled by 6 layers of muon chambers, represented by 1.5 cm of aluminium for each.

2. Endcap and forward region

The endcap and forward regions assume the same materials and thicknesses for the subsystems, with the EMCAL endcap extending from $z = 800$ cm to $z = 910$ cm and the HCAL end-cap from 910 cm to 1150 cm.

The acceptance of the forward region is assumed to start at $\eta = 2.5$, so the central system is cut in a cone-shaped volume along this angle. The forward dipole magnet extends from $z = 1500$ cm to $z = 2100$ cm and is assumed to be an aluminium cone enveloping the $\eta = 2.5$ cut and having about 60 cm wall thickness.

The forward tracking system consists of 6 equidistant discs placed between $z = 800$ cm and $z = 1500$ cm and 6 equidistant discs between $z = 2100$ cm and $z = 2400$ cm. Following the dipole, the forward tracking, ECAL, HCAL, Muon systems are placed at $z = 2100$, 2400, 2510, 2750 cm, respectively.

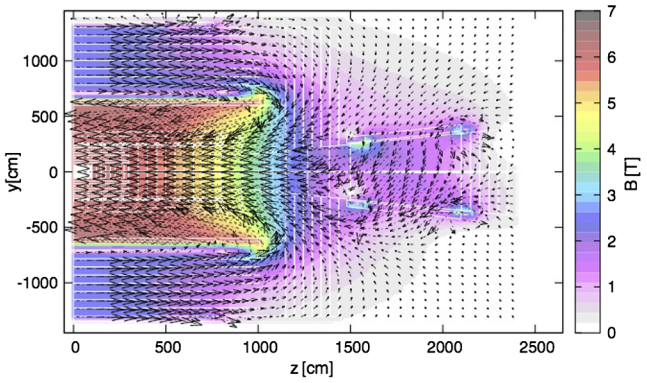

FIG. 2. Magnetic field map: lateral view for $x = 0$ [16].

B. Magnetic field

The magnetic field is the result of a superposition of a solenoid field directed along the z-axis and a dipole field along the y-axis. The central solenoid field is 6 T and the return field between the main coil and shielding coil is around 3 T. In the dipole region the field is not purely vertical and there is an up/down asymmetry. As it can be seen in Fig. 2, the field values are higher for positive y, because in this half plane the y-components of the solenoid and dipole fields have identical signs, while for $y < 0$ they have opposite signs.

III. SOURCE TERM CHARACTERIZATION

Proton-proton collisions have been simulated using the DPMJET-III generator [17,18], directly called from inside FLUKA. The assumed proton-proton nonelastic cross section, including inelastic scattering and single diffractive events, is 108 mbarn. The average number of particles generated in one collision is about 200. Moving away from the interaction point (IP), this multiform population evolves, even before touching the surrounding material, because of the decay of unstable particles (in particular neutral pions decaying into photon pairs). At 5 mm from the IP the average number of particles (neglecting neutrinos) is 256 and the main components are photons (almost 50%) and charged pions (38%). Neutral and charged kaons represent about the 7% of the total, while protons and neutrons are the 1.6% and 1.3% respectively. The remaining fraction consists of antiprotons and antineutrons (1% each) and hyperons.

Figure 3 shows the particle multiplicity as a function of pseudorapidity for 100 TeV p-p collisions compared to 14 TeV p-p collisions. Due to the larger center of mass energy, the average number of particles is expected to increase by a factor 1.8. The distribution is characterized by two symmetric peaks around $|\eta| = 1.5$ and about 80% of the particles are within the pseudorapidity coverage of the FCC detector, which is $-6 < \eta < 6$, as previously discussed. Despite this large coverage, most of the energy escapes from the detector. As it can be seen from Fig. 4, the energy distribution for p-p collisions at 100 TeV peaks at $|\eta|$ larger than 10 and the fraction of energy inside the detector acceptance is less than 5%. The total energy increase in the detector with respect to 14 TeV collisions is about a factor 4.5, considering for 14 TeV the pseudorapidity coverage of present ATLAS and CMS detector ($|\eta| < 5$). In the central region ($|\eta| < 2.5$) the energy increases only by a factor of 2.

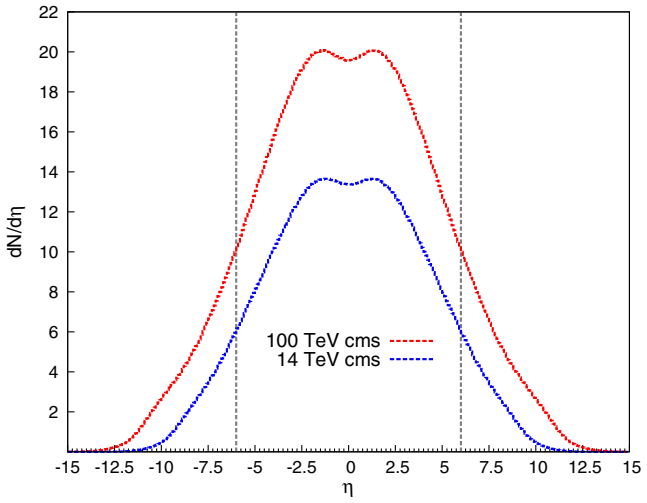

FIG. 3. Particle multiplicity as a function of pseudorapidity for 100 TeV p-p collisions in red and 14 TeV p-p collisions in blue at 5 mm from the nominal interaction point. The two vertical lines at $\eta = \pm 6$ show the detector acceptance.

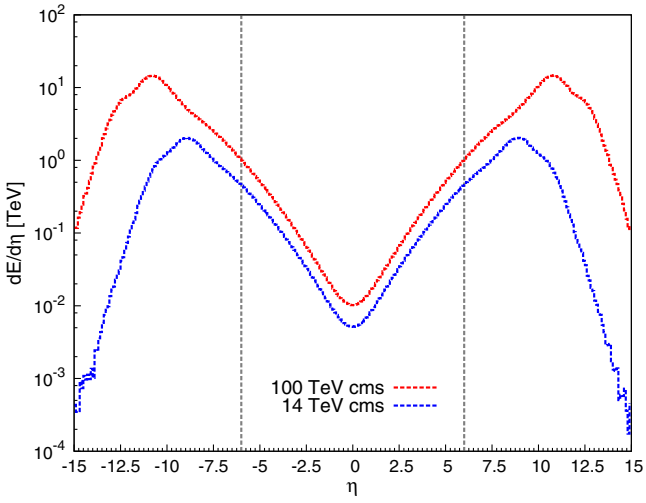

FIG. 4. Collision debris energy distribution as a function of pseudorapidity for 100 TeV p-p collisions in red and 14 TeV p-p collisions in blue at 5 mm from the nominal interaction point. The two vertical lines at $\eta = \pm 6$ show the detector acceptance.

IV. RADIATION CALCULATIONS

The load on the detector has been evaluated in terms of fluence rates, for the ultimate target instantaneous luminosity of 30×10^{34} cm^{-2} s^{-1}, to assess the detector occupancy. The long term damage has been estimated in terms of dose and 1 MeV neutron equivalent fluence, taking as reference the ultimate integrated luminosity of 30 ab^{-1}. An energy cutoff of 100 keV has been applied to all the particles, apart from electrons and positrons, for which a cutoff of 1 MeV is taken, and neutrons, which are considered down to thermal energies.

A. Fluence rates

1. Charged particle fluence rates

The distributions of the charged particle fluence rates are shown in Fig. 5 on the z-x plane at $y = 0$ and in Fig. 6 on the z-y plane at $x = 0$. The rates have a significant dependence on the radial distance from the beam line, but a weak dependence on z: as expected, equifluence lines are essentially parallel to the z-axis, certainly, in the central region. The distribution of charged particles is broader in the z-x plane, because of the effect of the dipole field directed along the y-axis. The latter is also visible in the z-y plane, where the higher fluence rate red line at $y > 0$ between 14 m and 17 m is due to electrons and positrons, which are captured by the magnetic field and curl around the field lines.

The charged particle fluence rates in the tracker are shown in Fig. 7 as a function of the distance from the beam line at different longitudinal positions: inside the barrel

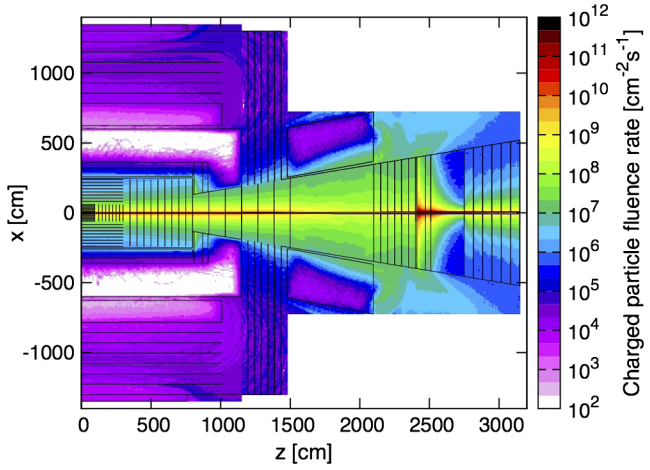

FIG. 5. Charged particle fluence rate for an instantaneous luminosity of 30×10^{34} cm^{-2} s^{-1}: top view. In the central region ($z < 10.5$ m) values are azimuthally averaged over 40 degrees around 0 (positive x) and π (negative x). In the forward region an average in the vertical direction around $y = 0$ is done on a bin of 1 cm up to $|x| = 0.6$ m and on a 10 cm bin for larger $|x|$ values. The origin of the coordinate system corresponds to the nominal collision point.

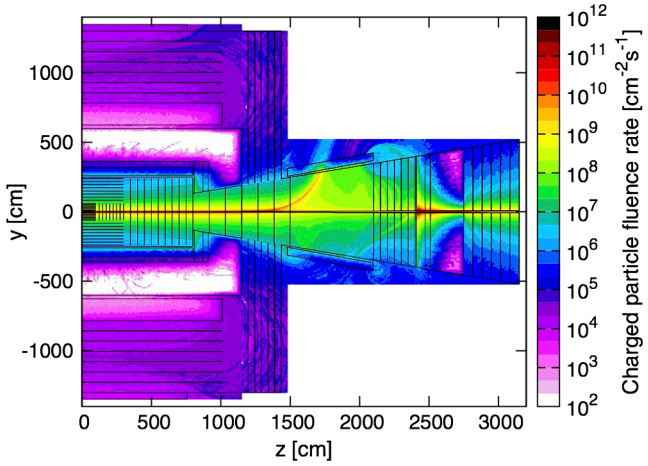

FIG. 6. Charged particle fluence rate for an instantaneous luminosity of 30×10^{34} cm^{-2} s^{-1}: lateral view. In the central region ($z < 10.5$ m) values are azimuthally averaged over 20 degrees around $\frac{\pi}{2}$ (positive y) and $-\frac{\pi}{2}$ (negative y). In the forward region an average in the horizontal direction around $x = 0$ is done on a bin of 1 cm up to $|y| = 0.6$ m and on a 10 cm bin for larger $|y|$ values.

tracker, in a forward tracking station before the dipole, in the tracking station closer to the forward calorimeters and in the forward muon spectrometer. The values in the tracker go from 2×10^{10} cm^{-2} s^{-1} in the first pixel layer to 10^6 cm^{-2} s^{-1} on its external side. The peak structure visible in the distribution at $z = 4$ m reflects the position of the

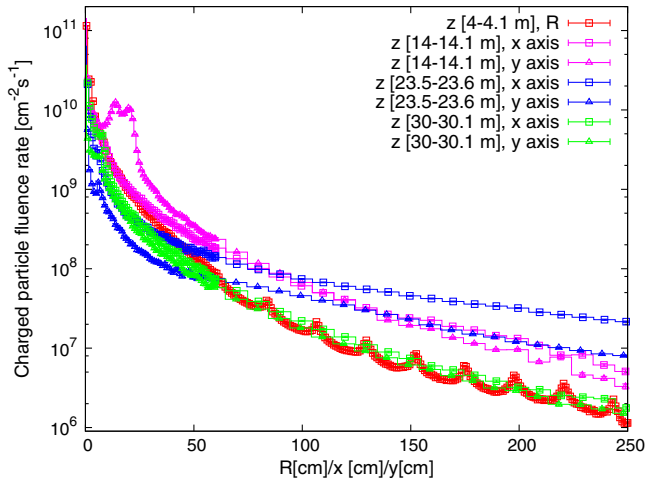

FIG. 7. Charged particle fluence rate for an instantaneous luminosity of 30×10^{34} cm^{-2} s^{-1} as a function of the distance from the beam line, at different z positions in the detector. In the central region the values are averaged on the azimuthal angle Φ and they are shown as a function of the radius R, while in the forward region they are shown as a function of x and y separately. The values as a function of x (y) are obtained with an average in the vertical (horizontal) direction on a bin of 1 cm around $y = 0$ ($x = 0$) up to $x\,(y) = 0.6$ m and on a bin of 10 cm for larger x (y) values.

cylindrical tracking stations in the barrel. The fluence distribution on the vertical plane at 14 m shows a bump, due to the above mentioned capture of electrons and positrons by the magnetic field. The effect of the latter is again visible in the fact that the fluence rates in the tracking station after the dipole are higher in the horizontal plane than in the vertical one. For radii greater than 60 cm, the values in the tracking station closer to the forward calorimeters are significantly higher than the ones in the barrel (up to ten times). This is due to backscattered particles from the forward calorimeters, where the fluence rate reaches 10^{11} cm^{-2} s^{-1}. From there, particles populate also the external part of the HADCAL and the muon spectrometer. The fluence rates are 2×10^5 cm^{-2} s^{-1} and above 10^6 cm^{-2} s^{-1} in the barrel and endcap muon chambers, respectively, more than 1000 times higher than the minimum reached in the barrel HADCAL. These values are too high for a good muon identification and need to be mitigated by proper shielding.

2. Neutron and photon fluence rates

The neutron fluence rate in the muon chambers reaches 10^8 cm^{-2} s^{-1}, causing a fake muon signal rate of 10^5 cm^{-2} s^{-1}, assuming that neutrons would have the same efficiency as in the resistive plate chambers of the ATLAS detector [19].

The photon fluence rate in the barrel and endcap muon chambers is shown in Fig. 8. The maximum values are 5×10^6 cm^{-2} s^{-1} and 10^8 cm^{-2} s^{-1} respectively, causing a background level analogous to the one of neutrons, assuming an efficiency of 1% as in the ATLAS muon chambers. These values are too high for a good muon identification and need to be reduced. As will be shown later in the paper, this can be achieved with a shielding around the forward calorimeters.

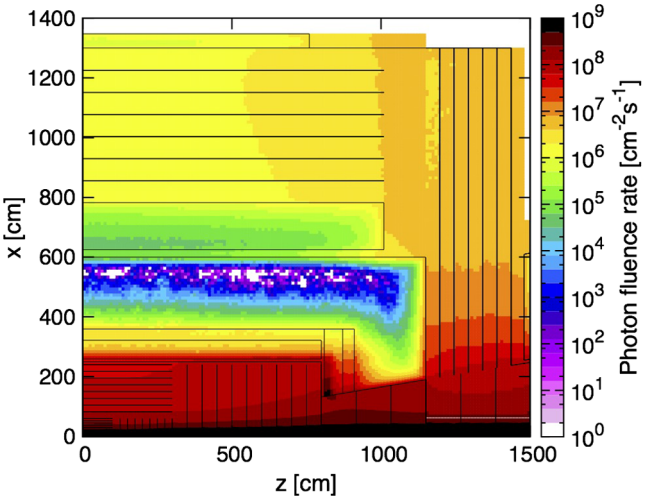

FIG. 8. Photon fluence rate for an instantaneous luminosity of 30×10^{34} cm^{-2} s^{-1}: top view, zoom on barrel and endcap muon chambers. The same scoring resolution as the one of Fig. 5 has been adopted, apart from the central region ($R < 2.5$ m and $|z| < 8$ m), where the considered radial resolution is 0.5 cm, instead of 1 cm.

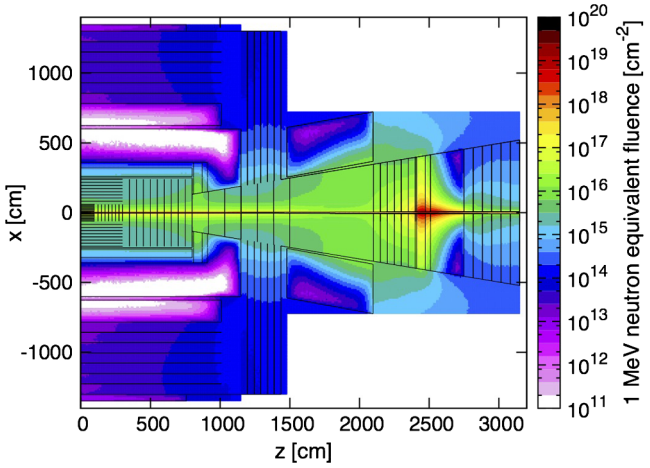

FIG. 9. 1 MeV neutron equivalent fluence for an integrated luminosity of 30 ab^{-1}: top view. The same scoring resolution as the one of Fig. 5 has been adopted, apart from the central region ($R < 2.5$ m and $|z| < 8$ m), where the considered radial resolution is 0.5 cm, instead of 1 cm.

B. Long term damage

1. 1 MeV neutron equivalent fluence

The distribution of the 1 MeV neutron equivalent fluence (relevant for silicon damage) is shown in Fig. 9 on the z-x plane at $y = 0$. As for fluence rate, a very strong dependence is observed as a function of R, while equifluence lines are to a good approximation parallel to the beam line.

Figure 10 shows the 1 MeV neutron equivalent fluence as a function of the distance from the beam axis, at the

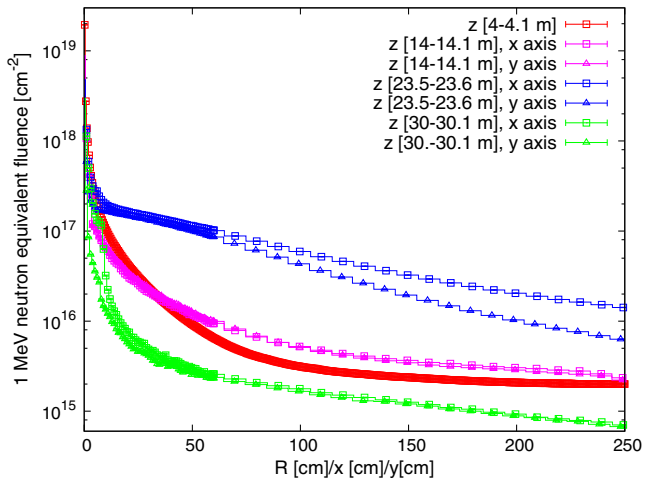

FIG. 10. 1 MeV neutron equivalent fluence after an integrated luminosity of 30 ab^{-1} as a function of the distance from the beam line, at different z positions in the detector, as in Fig. 7.

longitudinal positions already considered in Fig. 7. In the central region, at a radial distance below 50 cm, neutron fluence values exceed the ones expected at HL-LHC [10] by almost two orders of magnitude: we obtain $8\times10^{17}\,\mathrm{cm}^{-2}$ at the first pixel layer. In the tracking stations downstream of the dipole, the fluence is above 10^{16} cm^{-2} even at 2 m distance from the beam line, because of backscattering from the forward calorimeters. This represents a technological challenge, since present detectors cannot sustain values higher than 10^{16} cm^{-2} [20]. As expected, in this distribution on the vertical plane at 14 m there is no bump, while the distributions on the horizontal and vertical plane in the last tracking station are different. This is due to the direct contribution of charged particles (accounted for in the 1 MeV neutron equivalent fluence) and to the fact that secondary neutrons, produced by charged hadrons interactions in the forward calorimeters, have a broader distribution on the horizontal plane, reflecting the dipole field effect.

Figure 11 shows the fluence in the barrel and in the endcap calorimeters at different longitudinal positions. The fluence in the center of the detector at the entrance of the barrel EMCAL is above 10^{15} cm^{-2} and it is then reduced by the calorimeters by several orders of magnitude, down to 10^{10} cm^{-2} on the external side of the HADCAL. Values increase by almost two orders of magnitude in the gap between the calorimeter and the solenoid due to particles coming from the forward calorimeters. The distribution in the barrel at $z = 7.9$–8 m is very similar to the one at the center of the detector between $R = 3$ m and $R = 5.5$ m. For larger radii, the values are higher, because

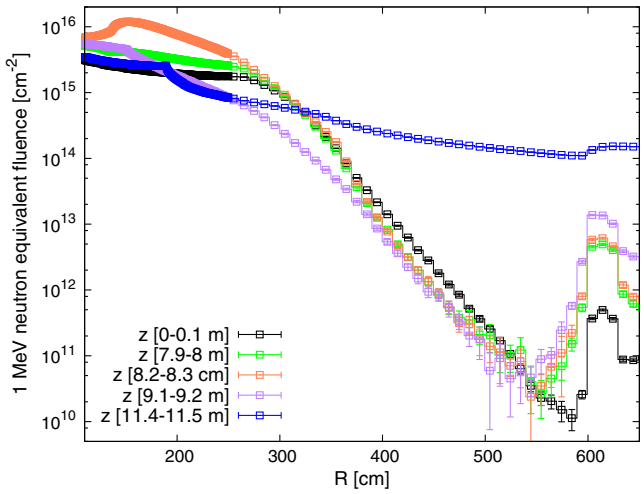

FIG. 11. 1 MeV neutron equivalent fluence after an integrated luminosity of 30 ab^{-1} as a function of the distance from the beam line, at different z positions in the calorimeters: at the detector center (black), at the end of the barrel (green), at the EMCAL endcap (orange), at the IP face HADCAL endcap (violet), and at the non-IP face of the HADCAL (blue). The values are averaged on the Φ angle.

the repopulation from the forward calorimeters is more important. The fluence rate in the gap reaches 5×10^{12} cm^{-2} and it is above 10^{13} cm^{-2} at the corresponding end-cap HADCAL position. The values on the inner side of the endcaps are higher than in the barrel, in particular in the EMCAL the fluence reaches 10^{16} cm^{-2}, while in the endcap HADCAL it is about 3×10^{15} cm^{-2}. The maximum on the non-IP side of the endcap HADCAL is lower, but here the values do not decrease significantly as a function of the radius, remaining above 10^{14} cm^{-2} up to beyond $R = 6$ m, because of the contribution from the forward calorimeters.

The values in the forward calorimeters are naturally even higher: the maximum fluence is 7×10^{18} cm^{-2} and above 4×10^{18} cm^{-2} in the EMCAL and HADCAL, respectively.

Finally, the fluence in the muon chambers reaches 10^{14} cm^{-2} in the barrel and 3×10^{15} cm^{-2} in the endcap, but they can be mitigated with the shielding discussed in Sec. V.

2. Dose

Figure 12 shows the dose distribution in the z-y plane. As for the charged particle fluence rate, the effect of the magnetic field is visible in the dipole region. The higher dose line in the $y > 0$ half-plane between 14 m and 17 m is due to electrons and positrons, which spiralize along the magnetic field lines. An analogous capture effect causes the higher dose line in the $y < 0$ half-plane between 20 m and 24 m, consistently with what can be observed in Fig. 6. The dose in the first pixel layer is 600 MGy, almost two orders of magnitude higher than what is expected at the HL-LHC [10]. It is reduced to 80 kGy at the entrance of the barrel EMCAL at $\eta = 0$ and it reaches a maximum of 120 kGy in this subdetector. The dose at the entrance of the HADCAL is 4 kGy and it reaches a minimum of 0.01 kGy. The values

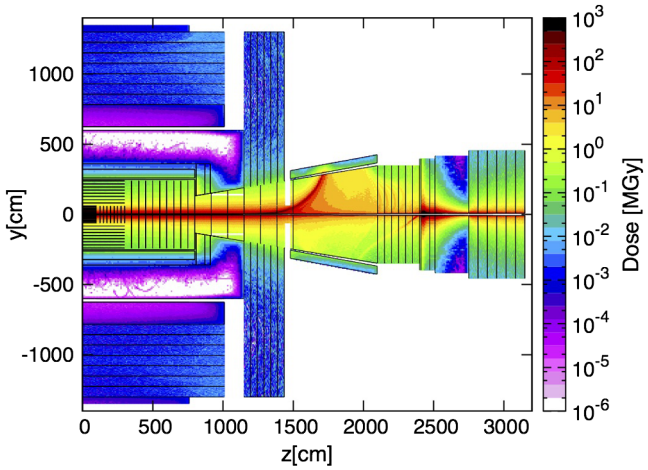

FIG. 12. Dose for an integrated luminosity of 30 ab^{-1}: lateral view. A dedicated scoring resolution has been used for the different subdetectors, adapted to their specific geometry.

in the HADCAL for $z > 10$ m are above 0.05 kGy, due to the contribution from particles coming from the forward calorimeters, where the dose values reach 10 GGy. While the values in the barrel HADCAL can be sustained by a scintillator detector, the maximum value in the endcap hadronic calorimeter is 0.4 MGy, which is excessive for this technology. Since the dose in the endcap at a radial distance greater than 3.6 m is 2 kGy, a possible solution is to have an extended barrel HADCAL based on scintillator technology up to $z = 11.5$ m with a radius larger than 3.6 m. The dose in this area is below few kGy, apart from the non-IP face of the HADCAL, where at 3.6 m it reaches 10 kGy. However this hot spot can be mitigated with a shielding. A different type of hadronic calorimeter, using for example LAr or silicon technology, is needed to cover the endcap HADCAL region for $R < 3.6$ m.

V. SHIELDING AND ITS EFFECTIVENESS

In order to protect the forward tracking stations and the muon chambers in the barrel and in the endcap from backscattering from the forward calorimeters, two shielding solutions have been considered to be put in front and around the forward calorimeters.

A. Shielding in front of the forward calorimeters

This shielding has been considered to protect the forward tracker. It is made of 5 cm of lithiated polyethylene, with a 2 mm thick cover of aluminium on both sides. The material choice aims at the neutron capture without gamma emission. This is achieved thanks to the presence of lithium. The effect of the shielding is clearly visible in the 1 MeV neutron equivalent fluence distribution as a function of distance from the beam line in three tracking stations in front of the forward calorimeters, shown in Fig. 13. On the two tracking layers closer to the calorimeters the fluence is reduced by up to a factor of three, while the impact on the tracking station upstream the dipole is less important, but still visible. Despite its limited thickness, the shielding is effective. However these values remain a technology challenge for silicon detectors.

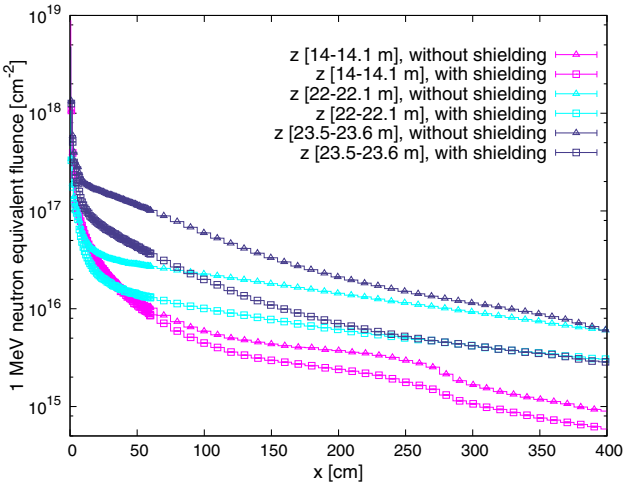

FIG. 13. 1 MeV neutron equivalent fluence as a function of x with (square) and without (triangle) shielding, at different z positions in the detector. The values are obtained with an average in the vertical direction on a bin of 1 cm around $y = 0$ up to $x = 0.6$ m and on a bin of 10 cm for larger x values.

B. Shielding around the forward calorimeters

A massive shielding can be put around the forward calorimeters up to the cavern wall, in order to protect the barrel and endcap muon chambers from backscattered particles. The shielding is composed of a 2 m thick iron wall to remove high energy particles. A 5 cm thick layer of lithiated polyethylene is put externally to further slow down and capture neutrons. Finally a 1 cm thick layer of lead is added as outer boundary, in order to absorb the capture photons, already made rare by the lithium presence.

Figure 14 shows the effect of the shielding on the neutron fluence rate, which is reduced by about four orders of magnitude in the relevant locations. Some neutron leakage can be seen at $z = 25$ m, at the level of the entrance of the electromagnetic forward calorimeter. In the barrel and endcap muon chambers one obtains about 10^3 cm^{-2} s^{-1} and 10^4 cm^{-2} s^{-1}, respectively, causing a maximum fake muon signal of 10 cm^{-2} s^{-1}. Figure 15 shows the photon fluence rate in the muon chambers on the z-x plane. The averaging over the azimuthal angle in the central region and over y in the forward region has been done on larger

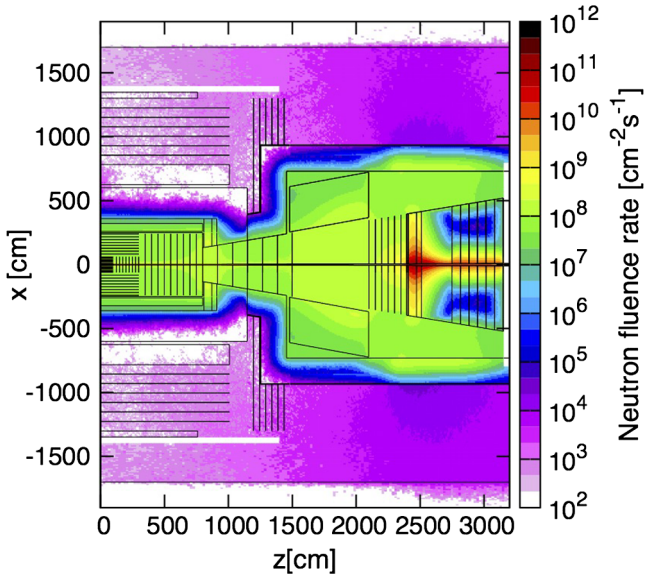

FIG. 14. Neutron fluence rate for an instantaneous luminosity of 30×10^{34} cm^{-2} s^{-1} in the presence of the shielding described in the text: top view. The same scoring resolution as the one of Fig. 9 has been adopted, except for the endcap muon chamber region, where the average on y has been done on a bin of about 1.3 m for $|x| > 0.6$ m.

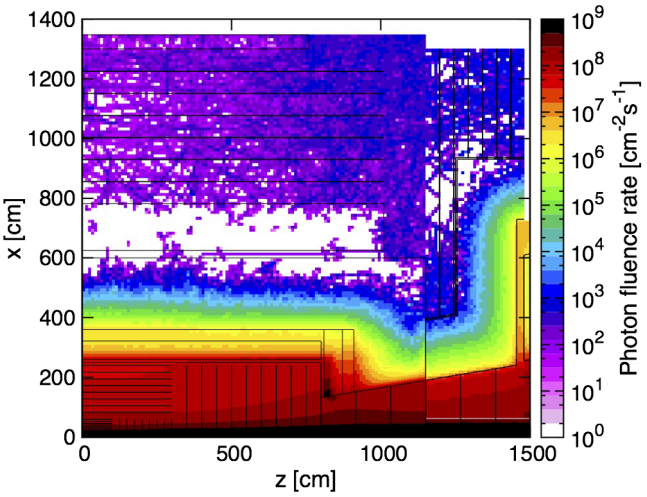

FIG. 15. Photon fluence rate for an instantaneous luminosity of 30×10^{34} cm^{-2} s^{-1} in the presence of the shielding described in the text: top view, zoom on the muon chambers. In the central region ($z < 10.5$ m) values are azimuthally averaged over 120 degrees around 0. In the forward region an average in the vertical direction around $y = 0$ is done on a bin of about 4.1 m (for $|x| > 0.6$ m).

intervals with respect to previous plots, to improve statistics. From the comparison with Fig. 8, the rate is reduced also in this case by four orders of magnitude and it reaches 10^3 cm^{-2} s^{-1} in the endcap, yielding a fake muon signal again of the order of 10 cm^{-2} s^{-1}. These values are comparable to the rates that can be afforded with present technologies and are currently observed in LHC experiments muon chambers.

VI. CONCLUSION

A first concept of a FCC detector has been implemented in FLUKA and the radiation load has been assessed in terms of fluence rates and long term damage relevant quantities. The 1 MeV neutron equivalent fluence values in the tracker are significantly higher than what is foreseen for HL-LHC, up to about two orders of magnitude. In particular, the values in the forward tracking stations are above 10^{16} cm^{-2} even in their external part (up to 2.5 m for the one closer to the calorimeter), because of the impact of the particles backscattered by the forward calorimeters. Currently, there are no technological solutions which can sustain such values, representing a clear challenge.

The estimated particle fluence rates, 1 MeV neutron equivalent fluence and dose values in the barrel are compatible with the choice of a LAr based HADCAL and a tile HADCAL, while the scintillator technology could not sustain the dose values foreseen in the endcap. A possible solution is to have an extended HADCAL barrel based on scintillator technology up to $z = 11.5$ m with a radius larger than 3.6 m and to use LAr technology for smaller radii. Finally, the obtained fluence rate values in the muon chambers in the barrel and in the endcap are too high for a good muon identification, because of particles backscattered from the forward calorimeters.

Based on these results, two different shielding systems have been conceived around and in front of the forward calorimeters to protect muon chambers and forward tracking stations. The resulting mitigation in the muon chambers is effective, reducing the neutron and photon fluence rates by about four orders of magnitude, down to manageable levels. For what concerns the forward tracking stations, the 1 MeV neutron equivalent fluence is reduced by up to a factor of three. Given the very limited amount of material (5 cm), the shielding is quite effective even if values remain challenging for present technologies.

In the future, the detector design is going to be further optimized to find the best compromise between cost and performance. Alternative options are under study, which will be evaluated along the same lines as discussed in this report.

ACKNOWLEDGMENTS

This work has profited from useful discussions within the FCC-hh Machine Detector Interface and FCC-hh Detector working groups.

[1] M. Benedikt and F. Zimmermann, Towards future circular colliders, J. Korean Phys. Soc. **69**, 893 (2016).
[2] M. Draper, in *Chamonix 2014: LHC Performance Workshop*, CERN (CERN, Geneva, 2015); organiser: Frédérick Bordry, Frank Zimmermann.
[3] G. Apollinari, I. Béjar Alonso, O. Brüning, M. Lamont, and L. Rossi, *High-Luminosity Large Hadron Collider (HL-LHC): Preliminary Design Report* (CERN, Geneva, 2015).
[4] A. Ferrari, P. R. Sala, A. Fassò, and J. Ranft, *FLUKA: A multi-particle transport code (program version 2005)* (CERN, Geneva, 2005).
[5] G. Battistoni *et al.*, Overview of the FLUKA code, Ann. Nucl. Energy **82**, 10 (2015).
[6] V. Boccone, R. Bruce, M. Brugger, M. Calviani, F. Cerutti, L. S. Esposito, A. Ferrari, A. Lechner, A. Mereghetti, E. Nowak, N. V. Shetty, E. Skordis, R. Versaci, and V. Vlachoudis, Beam-machine interaction at the CERN LHC, Nucl. Data Sheets **120**, 215 (2014).
[7] A. Airapetian *et al.* (ATLAS Collaboration), *ATLAS detector and physics performance: Technical Design Report, 1* (CERN, Geneva, 1999).
[8] S. Baranov, M. Bosman, I. Dawson, V. Hedberg, A. Nisati, and M. Shupe, CERN Reports No. ATL-GEN-2005-001, No. ATL-COM-GEN-2005-001, No. CERN-ATL-GEN-2005-001, 2005.
[9] G. L. Bayatian *et al.* (CMS Collaboration), *CMS Physics: Technical Design Report Volume 1: Detector Performance and Software* (CERN, Geneva, 2006).

[10] G. Aad *et al.* (ATLAS Collaboration), CERN Reports No. CERN-LHCC-2015-020, No. LHCC-G-166, 2015.
[11] D. Contardo, M. Klute, J. Mans, L. Silvestris, and J. Butler, CERN Reports No. CERN-LHCC-2015-010, No. LHCC-P-008, No. CMS-TDR-15-02, 2015.
[12] G. Ambrosio *et al.* (VLHC Design Study Group), SLAC Reports No. SLAC-R-591, No. FERMILAB-TM-2149, 2001.
[13] B. C. Barish *et al.* (GEM Collaboration), GEM Technical Design Report No. SSC-GEM-TN-93-262, 1993.
[14] R. Martin, M. I. Besana, F. Cerutti, and R. Tomás, Radiation Load Optimization in the Final Focus System of FCC-hh, in *Proceedings, 7th International Particle Accelerator Conference (IPAC 2016)* (JACoW, Geneva, 2016), p. TUPMW018.
[15] G. Aad *et al.* (ATLAS Collaboration), The ATLAS experiment at the CERN Large Hadron Collider, J. Instrum. **3**, S08003 (2008).
[16] M. Mentink and H. T. Kate (private communication).
[17] S. Roesler, R. Engel, and J. Ranft, The Monte Carlo event generator DPMJET-III, in *Advanced Monte Carlo for radiation physics, particle transport simulation and applications. Proceedings, Conference, MC2000, Lisbon, Portugal, 2000* (Springer, Berlin, Heidelberg, 2001), pp. 1033–1038.
[18] A. Fedynitch and R. Engel, Revision of the high energy hadronic interaction models PHOJET/DPMJET-II, in *Proceedings of 14th International Conference on Nuclear Reaction Mechanisms, Varenna, Italy, 2015* edited by F. Cerutti, M. Chadwick, A. Ferrari, T. Kawano, and P. Schoofs (CERN, Geneva, 2015), pp. 291–299.
[19] ATLAS Collaboration, *ATLAS muon spectrometer: Technical Design Report* (CERN, Geneva, 1997).
[20] I. Mandić, Silicon sensors for HL-LHC tracking detectors, Nucl. Instrum. Methods Phys. Res., Sect. A **732**, 126 (2013).